

High-fidelity, high-scalability two-qubit gate scheme for superconducting qubits

Yuan Xu,^{1,2,3,*} Ji Chu,⁴ Jiahao Yuan,⁵ Jiawei Qiu,⁵ Yuxuan Zhou,⁵ Libo Zhang,^{1,2,3}
Xinsheng Tan,^{4,†} Yang Yu,⁴ Song Liu,^{1,2,3} Jian Li,^{1,2,3,‡} Fei Yan,^{1,2,3,§} and Dapeng Yu^{1,2,3}

¹Shenzhen Institute for Quantum Science and Engineering,
Southern University of Science and Technology, Shenzhen, Guangdong, China

²Guangdong Provincial Key Laboratory of Quantum Science and Engineering,
Southern University of Science and Technology, Shenzhen, Guangdong, China

³Shenzhen Key Laboratory of Quantum Science and Engineering,
Southern University of Science and Technology, Shenzhen, Guangdong, China

⁴National Laboratory of Solid State Microstructures, Department of Physics, Nanjing University, Nanjing, Jiangsu, China

⁵Institute for Quantum Science and Engineering and Department of Physics,
Southern University of Science and Technology, Shenzhen, Guangdong, China

High-quality two-qubit gate operations are crucial for scalable quantum information processing. Often, the gate fidelity is compromised when the system becomes more integrated. Therefore, a low-error-rate, easy-to-scale two-qubit gate scheme is highly desirable. Here, we experimentally demonstrate a new two-qubit gate scheme that exploits fixed-frequency qubits and a tunable coupler in a superconducting quantum circuit. The scheme requires less control lines, reduces crosstalk effect, simplifies calibration procedures, yet produces a controlled- Z gate in 30 ns with a high fidelity of 99.5%, derived from the interleaved randomized benchmarking method. Error analysis shows that gate errors are mostly coherence limited. Our demonstration paves the way for large-scale implementation of high-fidelity quantum operations.

Quantum information processor architectures are scaling up at a fast pace, entering the Noisy Intermediate-Scale Quantum (NISQ) era [1–6]. The prospect of demonstrating quantum advantages with NISQ devices relies critically on continuing extending the system size without compromising the quality of quantum operations. Currently, two-qubit gate operation is the performance bottleneck in various modalities [7–10], and it generally deteriorates as more qubits, and hence more control lines, are integrated together. Obviously, more control lines introduce additional decohering channels, exacerbates crosstalk, and adds to the complexity of calibration procedures. Therefore, a high-fidelity yet easy-to-scale two-qubit gate scheme is the key to scalable quantum information processing.

For high-scalability two-qubit gates, two ingredients are highly desirable. First, the use of a tunable coupler between qubits has been proven effective in resolving the problem of frequency crowding, suppressing residual coupling, and enabling fast and high-fidelity two-qubit gates [2, 11–16]. However, humongous calibration efforts are required for precise control, especially when both qubits and couplers are tunable and sensitive to crosstalk [2]. The iterative and exquisite system tuning up adds instability to processor performance, hindering further scaling up. Second, fixed-frequency qubits can drastically simplify the system, require less control lines and have better coherence in general. Previous experiments have demonstrated these advantages with nontunable superconducting qubits made with single Josephson junction [17–21]. However, two-qubit interactions in these schemes are activated by parametrically driving the system, an inherently slow process that is prone to decohering errors. An ideal solution is a two-qubit gate scheme that takes advantage of both fixed-frequency qubits and tunable coupler, while maintaining high fidelity.

In this Letter, we experimentally demonstrate a new two-qubit gate scheme, compatible with fixed-frequency qubits, in a superconducting quantum circuit. Effective longitudinal qubit-qubit coupling can be adjusted by a single control parameter of a tunable coupler. With proper choice of the idling point, the system has a residual coupling strength as small as 20 kHz. Taking advantage of enhanced adiabaticity due to strong qubit-coupler coupling (> 100 MHz), we realize a fast (30 ns) and high-fidelity (99.5%) adiabatic controlled- Z (CZ) gate. Error analysis from separate measurements shows that the fidelity is limited mostly by decoherence. Moreover, our scheme is intrinsically robust against crosstalk and requires only a simple calibration sequence, promising better scalability in practice.

Our experiment is performed on a superconducting quantum circuit which consists of two Xmon qubits (Q_1, Q_2) [22] and a transmon-type [23] tunable coupler (C) in between, as shown in Fig. 1(a). Note that the first qubit is made tunable for another experimental purpose [24]. Throughout this Letter, it is biased at its maximum frequency, and can be treated as an equivalent of a fixed-frequency qubit. The system Hamiltonian can be expressed as

$$H/\hbar = \sum_{i=1,2,c} \omega_i a_i^\dagger a_i + \frac{\alpha_i}{2} a_i^\dagger a_i^\dagger a_i a_i + \sum_{i \neq j} g_{ij} (a_i^\dagger a_j + a_i a_j^\dagger), \quad (1)$$

where a_i^\dagger and a_i are corresponding creation and annihilation operators. $\omega_1/2\pi = 5.27$ GHz and $\omega_2/2\pi = 4.62$ GHz are the qubit frequencies. The coupler frequency ω_c is flux dependent, and is biased at $\omega_c/2\pi = 6.74$ GHz during idling and single-qubit gate periods. The corresponding anharmonicities are $\alpha_1/2\pi = -210$ MHz, $\alpha_2/2\pi = -240$ MHz, and $\alpha_c/2\pi = -370$ MHz. To speed up the two-qubit gate while

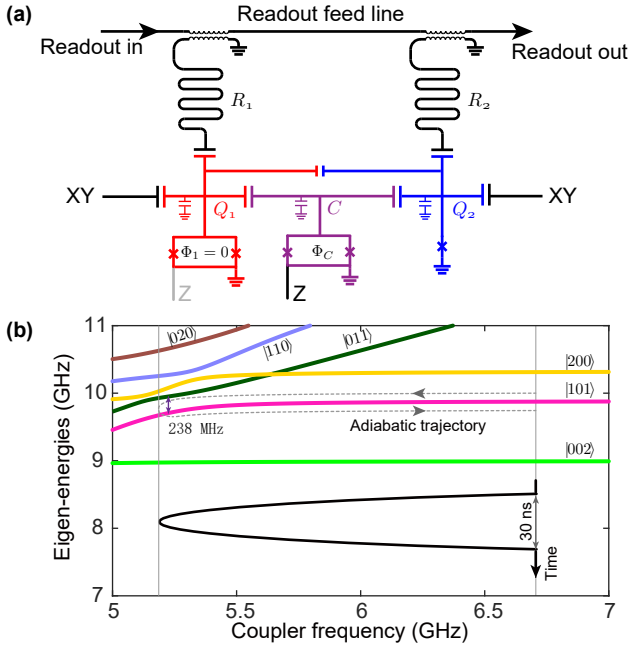


FIG. 1: Device schematic and concept of the adiabatic CZ gate. **(a)** Simplified circuit schematic of the experimental sample. The two qubits have a Xmon design, and the central tunable coupler is also a transmon-type qubit. The all-capacitive-coupling architecture allows convenient engineering of the nearest-neighbor and the weaker next-nearest-neighbor couplings. Single-qubit operations are implemented with local XY control lines. Two-qubit gates are implemented by modulating the magnetic flux threading the coupler’s superconducting quantum interference device loop Φ_C with the local Z control line. The first qubit is treated as an equivalent of a fixed-frequency qubit by setting its loop flux Φ_1 to zero throughout the experiment. Two $\lambda/4$ resonators, coupled to the same transmission line, are used for reading out the qubit states simultaneously. **(b)** System eigen-energies as a function of the coupler frequency. Only states in the two-excitation manifold are shown. The adiabatic CZ gate is realized by a 30-ns flux pulse applied to the coupler. The pulse assumes a simple half-period cosine shape. The gray dashed line indicates the adiabatic trajectory of an initial $|101\rangle$ state, which follows the pink level. The smallest gap between the pink state and the other states is about 238 MHz.

minimizing unwanted transitions, our design features enhanced coupling parameters. That is, $g_{12}/2\pi = 12$ MHz (between qubits), $g_{1c}/2\pi = 122$ MHz and $g_{2c}/2\pi = 105$ MHz (between qubit and coupler), much stronger than the conventional Xmon design [22]. More details about the device and experimental setup can be found in the Supplemental Material [25].

To illustrate how the adiabatic CZ gate is implemented, we may rewrite the system Hamiltonian in Eq. (1) using a generic form in its energy eigenbases ($|Q_1, C, Q_2\rangle$, labeled by the approximate bare states when the coupler is far detuned):

$$H'/\hbar = \tilde{\omega}_1 |100\rangle \langle 100| + \tilde{\omega}_2 |001\rangle \langle 001| + (\tilde{\omega}_1 + \tilde{\omega}_2 + \chi_{12}) |101\rangle \langle 101|, \quad (2)$$

after truncation to the computational subspace. The eigenen-

ergies $\tilde{\omega}_1$, $\tilde{\omega}_2$, and χ_{12} are all ω_c dependent. χ_{12} denotes the effective longitudinal coupling between qubits and is responsible for generating the entanglement. Finite χ_{12} is a consequence of interactions among higher levels, which can be relatively strong in transmon-type qubits due to their weak anharmonicity. The energy levels adjacent to $|101\rangle$ are plotted in Fig. 1(b) as a function of ω_c . In our two-qubit gate scheme, we adiabatically adjust the coupler from an idling bias to a region where the bare state $|101\rangle$ interacts more strongly with other levels and then back to the original bias. Nonzero χ_{12} during this process leads to a controlled-phase operation or a CZ gate if the total accumulated phase is π .

Note that when the coupler frequency is tuned down by the CZ pulse, the bare frequency of $|011\rangle$ has already crossed the level of $|101\rangle$ (i.e. $\omega_c < \omega_1$). However, we emphasize that the strong coupling between $|101\rangle$ and $|011\rangle$ is not the sole cause of χ_{12} , because $|011\rangle$ alone would have exactly the same level-pushing effect to $|101\rangle$ as $|010\rangle$ would do to $|100\rangle$, leading to a trivial single-qubit frequency shift. In fact, the nontrivial interaction mainly arises from couplings between $|101\rangle$ and second-excited states, which are $|200\rangle$, $|020\rangle$, and $|002\rangle$. These interactions may become much stronger when their interaction-mediating states, $|110\rangle$ and $|011\rangle$, are tuned close to them. In the specific device, $|020\rangle$ leads the contribution to χ_{12} , because $|020\rangle$ gets much closer to $|101\rangle$ in the interested regime than other second-excited states, given relatively larger anharmonicity of the coupler. The scheme may further benefit from optimizing the device parameters [28].

The adiabatic process is supposed to be slow enough to avoid unwanted transitions, e.g., leakage to noncomputational states [29]. In the conventional fixed-coupling architecture, the limit on the adiabatic CZ gate speed is set by the qubit-qubit coupling strength. In our device, with the introduction of a tunable coupler and its strong couplings to qubits, non-adiabatic effect can be effectively suppressed. The minimum gap between $|101\rangle$ and other states, a key factor in determining adiabaticity, is about 238 MHz, much greater than that in the conventional scheme. Also, we find that our scheme adds robustness in adiabaticity against parameter instability and pulse distortion [25]. Other non-adiabatic approaches that take advantage of the interference effect can facilitate the gate speed [30–32], but may become sensitive to pulse distortion, adding instability to gate performance.

In our experiment, we first measure the longitudinal coupling strength at different coupler frequencies, i.e., $\chi_{12}(\omega_c)$, from a conditional Ramsey-like experiment, as detailed in Fig. 2. The dynamic range of the longitudinal coupling strength spans more than 3 orders of magnitude, from 20 kHz to 100 MHz, enabling fast two-qubit gate operations as well as small residual coupling. The results are in good agreement with numerical simulation using our device parameters. Notably, since the two qubits have relatively large detuning ($|\omega_1 - \omega_2| > |\alpha_1|$), there is no working bias such that the coupling can be turned off completely. This is different from the case when the two qubits are prepared to be near resonance [2, 12]. However, we can still find a minimum coupling

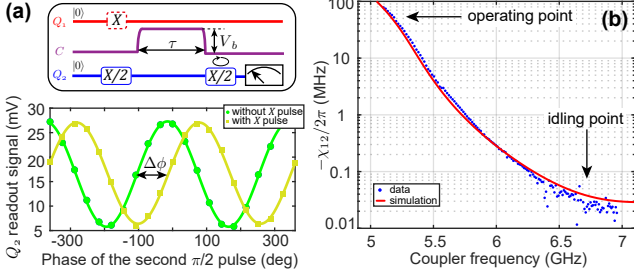


FIG. 2: Tunability of the longitudinal coupling. **(a)** In the top panel is the control sequence that performs a Ramsey-like sequence on Q_2 conditioning on the state of Q_1 in order to extract the longitudinal coupling. Between the two $\pi/2$ pulses applied to Q_2 , a squarelike flux pulse with amplitude V_b and duration τ is applied to the coupler. The phase shift induced by this pulse is captured by Q_2 with the Ramsey-like sequence. In our experiment, the phase of the last $\pi/2$ pulse is a varying parameter (indicated by the circling arrow) so that a full oscillation can be resolved, as shown in the bottom panel. Data (markers) are fitted (solid lines) by a sinusoidal function to extract the differential phase ($\Delta\phi$) between the cases of Q_1 being at the ground (green) or excited (yellow) state. **(b)** Effective longitudinal coupling strength χ_{12} as a function of the coupler frequency. χ_{12} can be derived from the previous results in (a) by the relation $\Delta\phi = \chi_{12}\tau$. The experiment is repeated with different pulse amplitudes V_b and fixed $\tau = 50\text{ns}$ (500ns) for larger (smaller) V_b . Together with separately measured coupler spectrum [25], we obtain $\chi_{12}(\omega_c)$ (blue dots), which is in good agreement with numerical results (red line). We choose $\omega_c/2\pi = 6.74$ GHz as the idling point in subsequent two-qubit gate experiments, due to the small residual coupling (20 kHz). Note that the negative of χ_{12} is plotted here.

that is small enough (20 kHz) for practical applications.

Next, we calibrate the adiabatic CZ gate. As shown in Fig. 1(b), the 30-ns flux pulse assumes a half-period cosine shape, with rising and falling edges smooth enough for adiabatic evolution at this timescale. A conditional Ramsey experiment similar to the one shown in Fig. 2(a) is used for calibrating the amplitude of the flux pulse, the only free parameter at this step. We obtain a CZ gate when the conditional phase shift satisfies $\Delta\phi = \pi$ and also find out the parasitic single-qubit phases, later to be compensated by virtual- Z gates [33]. For subsequent randomized benchmarking (RB) experiments, these parameters are further optimized using the RB results as the cost function [34].

We assess our gate performance by the conventional Clifford-based RB method [35–37], which measures the decay of the ground state probability (sequence fidelity) as a function of the number of two-qubit Cliffords m for both the reference and CZ-interleaved RB experiments, as shown in Fig. 3(a). With exponential fit, we obtain the average error per Clifford $r_{\text{ref}} = 0.0278$ and $r_{\text{int}} = 0.0328$. By comparing the exponential decay constants of the two traces, we extract the CZ gate fidelity $F_{\text{CZ}} = 1 - \frac{3}{4}(1 - p_{\text{int}}/p_{\text{ref}}) = 0.9948 \pm 0.0004$. We note that the difference in the trace offsets may result from leakage [25]. Since the ratio $r_{\text{CZ}}/r_{\text{ref}} \approx 0.18$ is small, there are possibilities of significant systematic variations in the interleaved RB results [38]. As a consistency

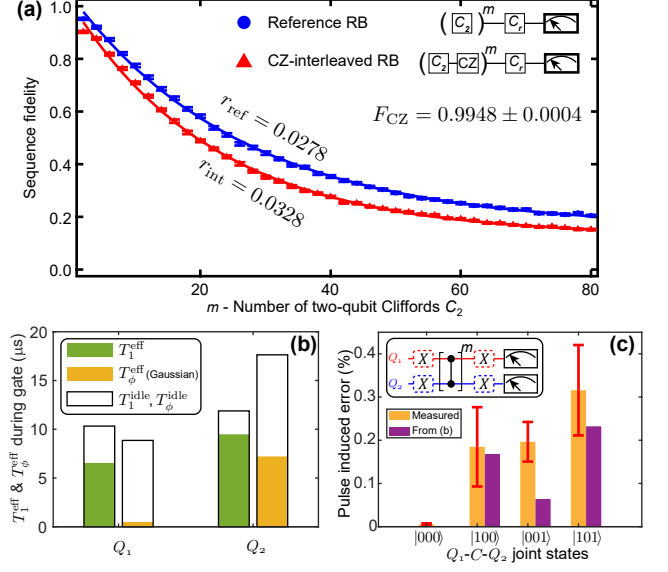


FIG. 3: Fidelity analysis of the adiabatic CZ gate. **(a)** Normalized sequence fidelity measured as a function of the number of Cliffords for both the reference (blue) and interleaved (red) RB experiments, with the sequences shown in the inset. Error bars on the data points are the standard deviations from the mean. We first obtain the decay constants, p_{ref} and p_{int} , from an exponential fit, $F = Ap^m + B$ (solid lines), and then derive the error rate per Clifford, r_{ref} and r_{int} from $r = \frac{3}{4}(1 - p)$. We also extract the CZ gate error from $r_{\text{CZ}} = \frac{3}{4}(1 - p_{\text{int}}/p_{\text{ref}})$ and finally the CZ gate fidelity $F_{\text{CZ}} = 1 - r_{\text{CZ}}$. The uncertainty of the fidelity is determined by bootstrapping. **(b)** Effective energy relaxation time T_1^{eff} (green bar) and pure dephasing (Gaussian decay) time T_ϕ^{eff} (orange bar) during the adiabatic CZ gate. The results are calculated by averaging over ω_c , weighted by the actual pulse shape (see Supplemental Material [25] for details). The blank outlines indicate measured characteristic times when the coupler is at the idling point. **(c)** Pulse-induced transitional errors by the CZ gate for different joint states (orange bars). Inset: control sequence. The qubits are prepared at the four different joint states with conditional π pulses. In each case, a varying number (m) of identical CZ gates are repeatedly applied. The final decay curves (versus m) are compared with a reference case in which CZ gates are replaced by identity gates of the same length, so that additional transition rates or errors due to the pulsing can be extracted (see [25] for details). The additional errors from the shortening of energy relaxation times during pulse are calculated by comparing the effective and idling T_1 times in (b) and shown for comparison (purple bars).

check, we rederive the CZ gate fidelity by subtracting single-qubit errors from the reference RB result using the relation $r_{\text{ref}} = 1.5r_{\text{CZ}} + 8.25r_{1q}$, where $r_{1q} = 0.0013$ [25]. The resulting error rate, 1.14%, sets an upper bound of the CZ gate fidelity.

To estimate the decoherence error, we first obtain the effective energy relaxation time T_1^{eff} and pure dephasing time T_ϕ^{eff} during the CZ gate [Fig. 3(b)]. Obviously, T_1^{eff} and T_ϕ^{eff} are lower than their counterparts during idling periods (T_1^{idle} and T_ϕ^{idle}). In particular, the higher-frequency Q_1 dephases drastically faster ($T_{\phi,Q_1}^{\text{eff}} \approx 0.5 \mu\text{s}$), a consequence of the

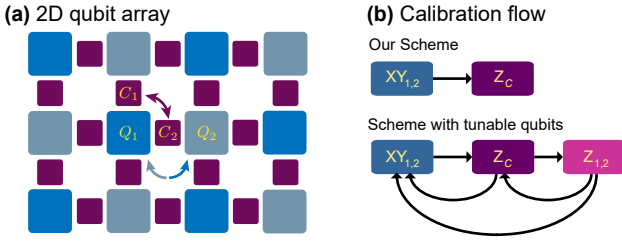


FIG. 4: Considerations on crosstalk and calibration. **(a)** Layout of a surface-code-compatible qubit array implementing our two-qubit gate scheme. Blue and gray squares denote qubits with different frequencies. The single-qubit (XY) control signals of two neighboring qubits (Q_1 and Q_2) have different frequency components, so their crosstalk has little influence on qubits. Although the two-qubit (Z) control signals applied to the tunable couplers (purple squares) share the same bandwidth, the flux crosstalk between neighboring couplers (C_1 and C_2) does not necessarily lead to adverse effect, because when the maximum frequency of the coupler is designed at the idling point (minimal residual coupling), an idling coupler becomes insensitive to flux, and also the longitudinal coupling is insensitive to the coupler frequency. Note that neighboring couplers can only be operated in turn in regular quantum circuits. **(b)** Comparison of the calibration flow. In our adiabatic CZ gate scheme, the qubit- XY signals (for single-qubit gate) are first calibrated before calibrating the coupler- Z signal (for two-qubit gate). In comparison, the iSWAP-like gate scheme [2] which requires stringent resonance condition between qubits demands iterative calibration procedures. For example, the qubit and coupler idling biases and control pulses have to be recalibrated once the other one is changed. The process may be further complicated by crosstalk and signal distortion.

stronger interaction between the qubit and the less coherent coupler during the CZ pulse. The (Gaussian) pure dephasing from Q_1 contributes $\frac{1}{3}(\tau_{\text{gate}}/T_{\phi,Q_1}^{\text{eff}})^2 = 0.12\%$ to gate errors [39], where $\tau_{\text{gate}} = 30$ ns is the pulse duration. The dephasing contribution from Q_2 ($\ll 0.01\%$) is negligible. The T_1 contribution to gate errors can be estimated by an empirical relation, $\frac{1}{3} \left(\frac{\tau_{\text{gate}}}{T_{1,Q_1}^{\text{eff}}} + \frac{\tau_{\text{gate}}}{T_{1,Q_2}^{\text{eff}}} + \frac{\tau_{\text{spacing}}}{T_{1,Q_1}^{\text{idle}}} + \frac{\tau_{\text{spacing}}}{T_{1,Q_2}^{\text{idle}}} \right) = 0.28\%$, where $\tau_{\text{spacing}} = 4$ ns is the interpulse spacing. Therefore, decoherence, including both T_1 and T_{ϕ} processes, accounts for about 77% of the total gate error, while pulse-induced nonadiabatic effects account for 23%, consistent with the numerical simulation result [25].

To validate our analysis, we perform a separate experiment, measuring the pulse-induced transitional errors on each of the four joint eigenstates, as detailed in Fig. 3(c) and the Supplemental Material [25]. Note that the extracted transition rates per gate denote the additional errors caused by the CZ pulse, compared to the identity operation. These errors include two parts, additional energy relaxation during gate and transitions caused by the pulse-induced dynamic effect, in this case, the nonadiabatic effect. The average difference between these rates and the T_1 contribution (orange versus purple bars in Fig. 3(c)), $(0.06 \pm 0.06)\%$, is hence the non-adiabatic errors, consistent with the above analysis.

Finally, we discuss the scalability of our scheme from

the perspective of crosstalk and calibration. Consider a 2D qubit array for implementing surface code [40], as shown in Fig. 4(a). With the problem of frequency crowding addressed by tunable couplers, we may pattern the qubit array with an interleaved frequency setup. Such an arrangement provides robustness against the XY -line crosstalk between neighboring qubits, because of the ineffectiveness of driving a qubit with a frequency-detuned signal. More importantly, our scheme is also intrinsically robust against the notorious Z -line crosstalk. Given that the maximum frequency of the coupler can be designed at the idling point (minimum residual coupling), the longitudinal coupling becomes doubly insensitive to flux variations, since both $\chi_{12}(\omega_c)$ and $\omega_c(\Phi_C)$ are at first order insensitive points. From our device parameters, it is estimated that a 10% flux crosstalk from the neighboring Z -line only incurs an additional coupling less than 1 kHz. The robustness against nearest-neighbor crosstalk in both types of control lines can provide more flexibility in signal routing in large-scale devices.

Compared to the state-of-the-art result using tunable qubits with tunable coupler [2], the calibration procedures for finding the optimized system and control parameters in our scheme are drastically simplified, as shown in Fig. 4(b). Since the qubits are fixed frequency and the couplers are insusceptible to crosstalk, the calibration process does not require iterative (cross) tuning-ups or complicated check procedures. Single- and two-qubit control parameters are calibrated separately in turn. The simplicity of our scheme not only reduces calibration procedures, but also adds stability to performance by lowering the probability of failure or bad events, enabling reliable chip-scale automated calibration.

To conclude, we experimentally demonstrate a new type of adiabatic CZ gate with fixed-frequency qubits and a tunable coupler in a superconducting quantum circuit. With a large on-off ratio (> 1000) of the effective coupling adjustable by the coupler frequency (flux), we achieve small residual coupling (20 kHz) and fast CZ gate (30 ns). A high gate fidelity of 99.5% is obtained from interleaved randomized benchmarking, with error analysis showing mostly coherence-limited gate error. The gate performance may further benefit from optimized pulse shape for faster adiabatic process [26] and from coherence improvement with new material platform [41]. Also, our scheme is easy to scale due to its intrinsic robustness against crosstalk and a simple calibration flow. This high-fidelity, high-scalability two-qubit gate scheme promises reproducibly high-quality quantum operations in future large-scale quantum information processors.

This work was supported by the Key-Area Research and Development Program of Guangdong Province (Grant No. 2018B030326001), the National Natural Science Foundation of China (Grant No. U1801661), the Guangdong Provincial Key Laboratory (Grant No. 2019B121203002), the Guangdong Innovative and Entrepreneurial Research Team Program (Grant No. 2016ZT06D348), the Natural Science Foundation of Guangdong Province (Grant No. 2017B030308003) and the Science, Technology and Innovation Commission of Shen-

zhen Municipality (Grants No. JCYJ20170412152620376, No. KYTDPT20181011104202253). J.L. acknowledges support from the National Natural Science Foundation of China (Grant No. 11874065) and the Natural Science Foundation of Hunan Province (Grant No. 2018JJ1031). Y.X. acknowledges support from the Youth Project of National Natural Science Foundation of China (Grant No. 11904158). Y.Y. acknowledges support from the National Key Research and Development Program of China (Grant No. 2016YFA0301802).

Y. X. and J. C. contributed equally to this work.

Note added.— We notice concurrent development of a similar work to implement conditional-phase gates with a tunable coupler [42].

* Electronic address: xuy5@sustech.edu.cn

† Electronic address: tanxs@nju.edu.cn

‡ Electronic address: lj33@sustech.edu.cn

§ Electronic address: yanf2020@mail.sustech.edu.cn

- [1] J. Preskill, “Quantum Computing in the NISQ era and beyond,” *Quantum* **2**, 79 (2018).
- [2] F. Arute, K. Arya, R. Babbush, D. Bacon, J. C. Bardin, R. Barends, R. Biswas, S. Boixo, F. G. S. L. Brandao, D. A. Buell, *et al.*, “Quantum supremacy using a programmable superconducting processor,” *Nature* **574**, 505 (2019).
- [3] J. S. Otterbach, R. Manenti, N. Alidoust, A. Bestwick, M. Block, B. Bloom, S. Caldwell, N. Didier, E. S. Fried, S. Hong, *et al.*, “Unsupervised Machine Learning on a Hybrid Quantum Computer,” [arXiv: 1712.05771](https://arxiv.org/abs/1712.05771) (2017).
- [4] A. Omran, H. Levine, A. Keesling, G. Semeghini, T. T. Wang, S. Ebadi, H. Bernien, A. S. Zibrov, H. Pichler, S. Choi, J. Cui, M. Rossignolo, P. Rembold, S. Montangero, T. Calarco, M. Endres, M. Greiner, V. Vuletić, and M. D. Lukin, “Generation and manipulation of schrödinger cat states in rydberg atom arrays,” *Science* **365**, 570 (2019).
- [5] C. Song, K. Xu, H. Li, Y.-R. Zhang, X. Zhang, W. Liu, Q. Guo, Z. Wang, W. Ren, J. Hao, H. Feng, H. Fan, D. Zheng, D.-W. Wang, H. Wang, and S.-Y. Zhu, “Generation of multicomponent atomic schrödinger cat states of up to 20 qubits,” *Science* **365**, 574 (2019).
- [6] Z. Yan, Y.-R. Zhang, M. Gong, Y. Wu, Y. Zheng, S. Li, C. Wang, F. Liang, J. Lin, Y. Xu, C. Guo, L. Sun, C.-Z. Peng, K. Xia, H. Deng, H. Rong, J. Q. You, F. Nori, H. Fan, X. Zhu, and J.-W. Pan, “Strongly correlated quantum walks with a 12-qubit superconducting processor,” *Science* **364**, 753 (2019).
- [7] D. M. Zajac, A. J. Sigillito, M. Russ, F. Borjans, J. M. Taylor, G. Burkard, and J. R. Petta, “Resonantly driven cnot gate for electron spins,” *Science* **359**, 439 (2018).
- [8] K. Wright, K. M. Beck, S. Debnath, J. M. Amini, Y. Nam, N. Grzesiak, J.-S. Chen, N. C. Panti, M. Chmielewski, C. Collins, *et al.*, “Benchmarking an 11-qubit quantum computer,” *Nat. Commun.* **10**, 5464 (2019).
- [9] Y. He, S. K. Gorman, D. Keith, L. Kranz, J. G. Keizer, and M. Y. Simmons, “A two-qubit gate between phosphorus donor electrons in silicon,” *Nature* **571**, 371 (2019).
- [10] M. Kjaergaard, M. E. Schwartz, A. Greene, G. O. Samach, A. Bengtsson, M. O’Keefe, C. M. McNally, J. Braumüller, D. K. Kim, P. Krantz, *et al.*, “A quantum instruction set implemented on a superconducting quantum processor,” [arXiv: 2001.08838](https://arxiv.org/abs/2001.08838) (2020).
- [11] Y. Chen, C. Neill, P. Roushan, N. Leung, M. Fang, R. Barends, J. Kelly, B. Campbell, Z. Chen, B. Chiaro, *et al.*, “Qubit architecture with high coherence and fast tunable coupling,” *Phys. Rev. Lett.* **113**, 220502 (2014).
- [12] F. Yan, P. Krantz, Y. Sung, M. Kjaergaard, D. L. Campbell, T. P. Orlando, S. Gustavsson, and W. D. Oliver, “Tunable coupling scheme for implementing high-fidelity two-qubit gates,” *Phys. Rev. Applied* **10**, 054062 (2018).
- [13] P. Mundada, G. Zhang, T. Hazard, and A. Houck, “Suppression of qubit crosstalk in a tunable coupling superconducting circuit,” *Phys. Rev. Applied* **12**, 054023 (2019).
- [14] X. Li, T. Cai, H. Yan, Z. Wang, X. Pan, Y. Ma, W. Cai, J. Han, Z. Hua, X. Han, *et al.*, “Tunable coupler for realizing a controlled-phase gate with dynamically decoupled regime in a superconducting circuit,” *Phys. Rev. Applied* **14**, 024070 (2020).
- [15] X. Y. Han, T. Q. Cai, X. G. Li, Y. K. Wu, Y. W. Ma, Y. L. Ma, J. H. Wang, H. Y. Zhang, Y. P. Song, and L. M. Duan, “Error analysis in suppression of unwanted qubit interactions for a parametric gate in a tunable superconducting circuit,” *Phys. Rev. A* **102**, 022619 (2020).
- [16] B. Foxen, C. Neill, A. Dunsworth, P. Roushan, B. Chiaro, A. Megrant, J. Kelly, Z. Chen, K. Satzinger, R. Barends, *et al.*, “Demonstrating a Continuous Set of Two-qubit Gates for Near-term Quantum Algorithms,” *Phys. Rev. Lett.* **125**, 120504 (2020).
- [17] J. M. Chow, A. D. Córcoles, J. M. Gambetta, C. Rigetti, B. R. Johnson, J. A. Smolin, J. R. Rozen, G. A. Keefe, M. B. Rothwell, M. B. Ketchen, and M. Steffen, “Simple all-microwave entangling gate for fixed-frequency superconducting qubits,” *Phys. Rev. Lett.* **107**, 080502 (2011).
- [18] D. C. McKay, S. Filipp, A. Mezzacapo, E. Magesan, J. M. Chow, and J. M. Gambetta, “Universal gate for fixed-frequency qubits via a tunable bus,” *Phys. Rev. Applied* **6**, 064007 (2016).
- [19] S. A. Caldwell, N. Didier, C. A. Ryan, E. A. Sete, A. Hudson, P. Karalekas, R. Manenti, M. P. da Silva, R. Sinclair, E. Acala, N. Alidoust, *et al.*, “Parametrically activated entangling gates using transmon qubits,” *Phys. Rev. Appl.* **10**, 034050 (2018).
- [20] A. Bengtsson, P. Vikstål, C. Warren, M. Svensson, X. Gu, A. F. Kockum, P. Krantz, C. Križan, D. Shiri, I.-M. Svensson, *et al.*, “Improved success probability with greater circuit depth for the quantum approximate optimization algorithm,” *Phys. Rev. Applied* **14**, 034010 (2020).
- [21] M. S. Blok, V. V. Ramasesh, T. Schuster, K. O’Brien, J. Kreikebaum, D. Dahlen, A. Morvan, B. Yoshida, N. Y. Yao, and I. Siddiqi, “Quantum Information Scrambling in a Superconducting Qutrit Processor,” [arXiv: 2003.03307](https://arxiv.org/abs/2003.03307) (2020).
- [22] R. Barends, J. Kelly, A. Megrant, D. Sank, E. Jeffrey, Y. Chen, Y. Yin, B. Chiaro, J. Mutus, C. Neill, *et al.*, “Coherent josephson qubit suitable for scalable quantum integrated circuits,” *Phys. Rev. Lett.* **111**, 080502 (2013).
- [23] J. Koch, T. M. Yu, J. Gambetta, A. A. Houck, D. I. Schuster, J. Majer, A. Blais, M. H. Devoret, S. M. Girvin, and R. J. Schoelkopf, “Charge-insensitive qubit design derived from the Cooper pair box,” *Phys. Rev. A* **76**, 042319 (2007).
- [24] J. Qiu *et al.*, in preparation. (2020).
- [25] See Supplemental Material [url] for a discussion of the device, enhanced adiabaticity, and error analysis, which includes Refs. [10, 14, 26, 27].
- [26] J. M. Martinis and M. R. Geller, “Fast adiabatic qubit gates using only σ_z control,” *Phys. Rev. A* **90**, 022307 (2014).
- [27] R. Barends, J. Kelly, A. Megrant, A. Veitia, D. Sank, E. Jeffrey, T. C. White, J. Mutus, A. G. Fowler, B. Campbell, *et al.*, “Superconducting quantum circuits at the surface code threshold

- for fault tolerance,” *Nature* **508**, 500 (2014).
- [28] J. Chu *et al.*, in preparation. (2020).
- [29] L. DiCarlo, J. M. Chow, J. M. Gambetta, L. S. Bishop, B. R. Johnson, D. I. Schuster, J. Majer, A. Blais, L. Frunzio, S. M. Girvin, and R. J. Schoelkopf, “Demonstration of two-qubit algorithms with a superconducting quantum processor,” *Nature* **460**, 240 (2009).
- [30] M. A. Rol, F. Battistel, F. K. Malinowski, C. C. Bultink, B. M. Tarasinski, R. Vollmer, N. Haider, N. Muthusubramanian, A. Bruno, B. M. Terhal, and L. DiCarlo, “Fast, high-fidelity conditional-phase gate exploiting leakage interference in weakly anharmonic superconducting qubits,” *Phys. Rev. Lett.* **123**, 120502 (2019).
- [31] S. Li, A. D. Castellano, S. Wang, Y. Wu, M. Gong, Z. Yan, H. Rong, H. Deng, C. Zha, C. Guo, *et al.*, “Realisation of high-fidelity nonadiabatic CZ gates with superconducting qubits,” *npj Quantum Inf.* **5**, 84 (2019).
- [32] R. Barends, C. M. Quintana, A. G. Petukhov, Y. Chen, D. Kafri, K. Kechedzhi, R. Collins, O. Naaman, S. Boixo, F. Arute, *et al.*, “Diabatic gates for frequency-tunable superconducting qubits,” *Phys. Rev. Lett.* **123**, 210501 (2019).
- [33] D. C. McKay, C. J. Wood, S. Sheldon, J. M. Chow, and J. M. Gambetta, “Efficient z gates for quantum computing,” *Phys. Rev. A* **96**, 022330 (2017).
- [34] J. Kelly, R. Barends, B. Campbell, Y. Chen, Z. Chen, B. Chiaro, A. Dunsworth, A. G. Fowler, I.-C. Hoi, E. Jeffrey, *et al.*, “Optimal quantum control using randomized benchmarking,” *Phys. Rev. Lett.* **112**, 240504 (2014).
- [35] E. Knill, D. Leibfried, R. Reichle, J. Britton, R. B. Blakestad, J. D. Jost, C. Langer, R. Ozeri, S. Seidelin, and D. J. Wineland, “Randomized benchmarking of quantum gates,” *Phys. Rev. A* **77**, 012307 (2008).
- [36] E. Magesan, J. M. Gambetta, and J. Emerson, “Scalable and robust randomized benchmarking of quantum processes,” *Phys. Rev. Lett.* **106**, 180504 (2011).
- [37] E. Magesan, J. M. Gambetta, B. R. Johnson, C. A. Ryan, J. M. Chow, S. T. Merkel, M. P. da Silva, G. A. Keefe, M. B. Rothwell, T. A. Ohki, M. B. Ketchen, and M. Steffen, “Efficient measurement of quantum gate error by interleaved randomized benchmarking,” *Phys. Rev. Lett.* **109**, 080505 (2012).
- [38] J. M. Epstein, A. W. Cross, E. Magesan, and J. M. Gambetta, “Investigating the limits of randomized benchmarking protocols,” *Phys. Rev. A* **89**, 062321 (2014).
- [39] P. J. J. O’Malley, J. Kelly, R. Barends, B. Campbell, Y. Chen, Z. Chen, B. Chiaro, A. Dunsworth, A. G. Fowler, I.-C. Hoi, E. Jeffrey, A. Megrant, J. Mutus, C. Neill, C. Quintana, P. Roushan, D. Sank, A. Vainsencher, J. Wenner, T. C. White, A. N. Korotkov, A. N. Cleland, and J. M. Martinis, “Qubit metrology of ultralow phase noise using randomized benchmarking,” *Phys. Rev. Applied* **3**, 044009 (2015).
- [40] A. G. Fowler, M. Mariantoni, J. M. Martinis, and A. N. Cleland, “Surface codes: Towards practical large-scale quantum computation,” *Phys. Rev. A* **86**, 032324 (2012).
- [41] A. P. M. Place, L. V. H. Rodgers, P. Mundada, B. M. Smitham, M. Fitzpatrick, Z. Leng, A. Premkumar, J. Bryon, S. Sussman, G. Cheng, T. Madhavan, H. K. Babla, B. Jaeck, A. Gyenis, N. Yao, R. J. Cava, N. P. de Leon, and A. A. Houck, “New material platform for superconducting transmon qubits with coherence times exceeding 0.3 milliseconds,” [arXiv: 2003.00024](https://arxiv.org/abs/2003.00024) (2020).
- [42] M. C. Collodo, J. Herrmann, N. Lacroix, C. K. Andersen, A. Remm, S. Lazar, J.-C. Besse, T. Walter, A. Wallraff, and C. Eichler, “Implementation of Conditional-Phase Gates based on tunable ZZ-Interactions,” [arXiv: 2005.08863](https://arxiv.org/abs/2005.08863) (2020).

Supplementary Material for
“High-fidelity, high-scalability two-qubit gate scheme for superconducting qubits”

Yuan Xu,^{1,2,3,*} Ji Chu,⁴ Jiahao Yuan,⁵ Jiawei Qiu,⁵ Yuxuan Zhou,⁵ Libo Zhang,^{1,2,3}
Xinsheng Tan,^{4,†} Yang Yu,⁴ Song Liu,^{1,2,3} Jian Li,^{1,2,3,‡} Fei Yan,^{1,2,3,§} and Dapeng Yu^{1,2,3}

¹*Shenzhen Institute for Quantum Science and Engineering,
Southern University of Science and Technology, Shenzhen, Guangdong, China*

²*Guangdong Provincial Key Laboratory of Quantum Science and Engineering,
Southern University of Science and Technology, Shenzhen, Guangdong, China*

³*Shenzhen Key Laboratory of Quantum Science and Engineering,
Southern University of Science and Technology, Shenzhen, Guangdong, China*

⁴*National Laboratory of Solid State Microstructures, Department of Physics, Nanjing University, Nanjing, Jiangsu, China*

⁵*Institute for Quantum Science and Engineering and Department of Physics,
Southern University of Science and Technology, Shenzhen, Guangdong, China*

*Electronic address: xuy5@sustech.edu.cn

†Electronic address: tanxs@nju.edu.cn

‡Electronic address: lij33@sustech.edu.cn

§Electronic address: yanf2020@mail.sustech.edu.cn;

Y. X. and J. C. contributed equally to this work.

I. THE DEVICE

A. Device parameters and experimental setup

The device is fabricated with aluminum on sapphire substrate. Relevant device parameters are summarized in Table S1. The device is mounted inside a dilution refrigerator at a base temperature of about 10 mK. Fridge wiring and measurement circuitry are shown in Fig. S1. We perform the standard circuit-QED measurements.

TABLE S1: Device parameters.

Parameters (MHz)	Q_1	Q_2
Resonator frequency ($\omega_{R1}/2\pi$, $\omega_{R2}/2\pi$)	6955	7002
Qubit frequency ($\omega_1/2\pi$, $\omega_2/2\pi$)	5271	4615
Qubit anharmonicity ($\alpha_1/2\pi$, $\alpha_2/2\pi$)	-210	-240
Coupler frequency (idling)	6704	
Coupler anharmonicity ($\alpha_c/2\pi$)	-370	
Qubit-coupler coupling ($g_{1c}/2\pi$, $g_{2c}/2\pi$)	122	105
Qubit-qubit direct coupling ($g_{12}/2\pi$)	12	
Single-qubit gate fidelity	99.84%	99.90%
Readout fidelity	86%	85%

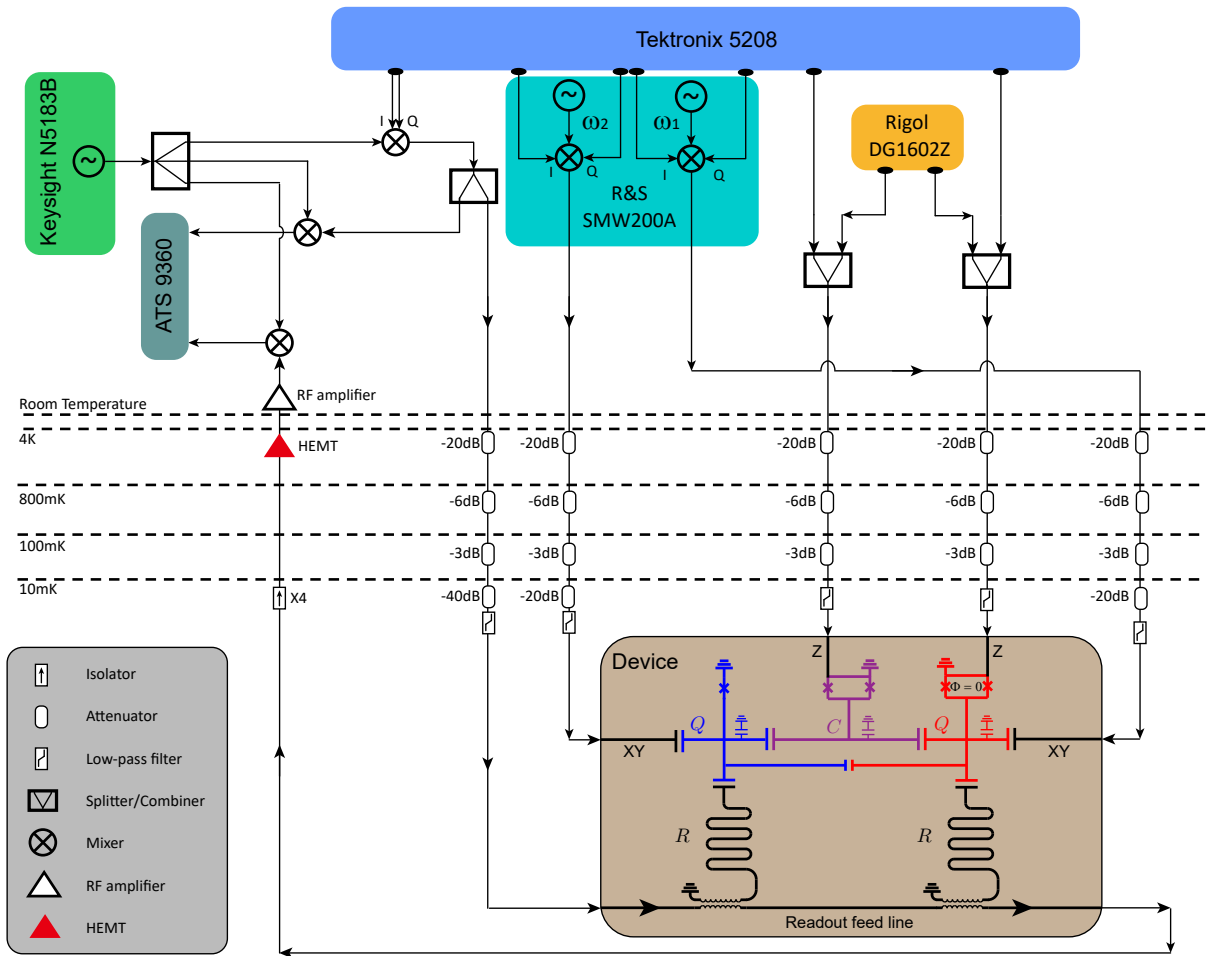


FIG. S1: Wiring diagram and circuit components.

B. Z crosstalk

In order to use the first qubit Q_1 (tunable) as a fixed-frequency qubit, its flux bias has to be set to zero throughout the experiment. Therefore, we characterize and compensate crosstalk of Z control lines between Q_1 and the coupler. The crosstalk coefficients (about 8%) are derived from measuring the frequency response to the control lines. However, when Q_1 is biased at its maximum frequency as in all subsequent experiments, its frequency becomes insensitive to flux variation, adding extra robustness against crosstalk. Therefore, it is valid to treat Q_1 as a fixed-frequency qubit in our experiment.

C. Coupler spectrum

Due to strong coupling between Q_2 and the coupler, there is a frequency shift of Q_2 depending on the coupler state. We take advantage of this effect to measure the spectrum of the coupler [1]. The pulse sequence and the measured results are shown in Fig. S2. The two visible avoided crossings correspond to the couplings between the coupler and the two qubits, from which the coupling strengths g_{1c} and g_{2c} can be extracted.

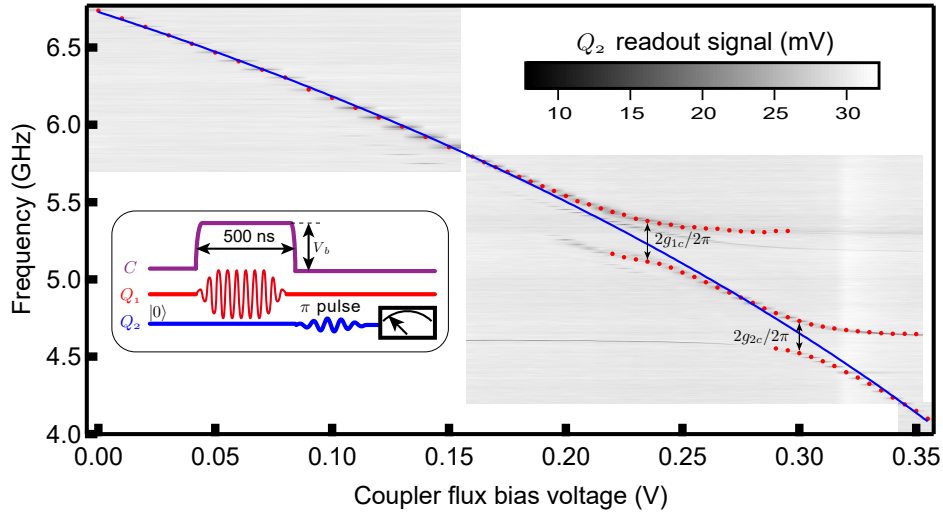


FIG. S2: Measured coupler spectrum with corresponding pulse sequence (inset). The coupler is pulse-biased away from the idling point to a varying amplitude V_b while driven by a microwave pulse applied to the XY control line of Q_1 . Transitions occur when the drive frequency is on resonance with the pulse-biased coupler frequency. Due to strong coupling between the coupler and Q_2 , a coupler-state-dependent frequency shift of Q_2 can be used to distinguish the coupler state by probing R_2 after a selective π -pulse on Q_2 . On the greyed color plot, red dashed lines are the measured transitions and the blue solid line is the bare coupler spectrum from fit. The smallest gaps of the two avoided crossings indicate twice the coupling strength.

The coherence of the coupler may be inferred from its spectral width which is about 10 MHz, equivalent to a T_2 time of a few tens of nanoseconds. However, this is very rough estimate, because the spectral width is broadened by the drive. Also, it is important to distinguish the device's local noise from instability of control instrumentation. In general, the AWG used for pulsing the coupler adds extra low-frequency noise. In separate tests, we find that this could limit qubit coherence to only a few hundred nanoseconds.

II. ENHANCED ADIABATICITY

In general, the adiabatic condition in an adiabatic process between any two states, $|m\rangle$ and $|n\rangle$, is defined by the relation:

$$\beta_{nm} = \left| \frac{\hbar \langle n | \partial H / \partial t | m \rangle}{(E_n - E_m)^2} \right| = \left| \frac{\hbar \langle n | \dot{m} \rangle}{E_m - E_n} \right| \ll 1, n \neq m. \quad (\text{S1})$$

β_{nm} quantifies the unwanted transitions. Here, we compare two protocols of adiabatic CZ gate, modulating the frequency of tunable qubits in the conventional fixed-coupling architecture [2, 3] and modulating the frequency of the tunable coupler as done in our work. Summing over all the possible states to which the population transfer, we can rewrite Eq. S1 as

$$\beta_m = \sum_{n \neq m} \left| \frac{\hbar \langle n | \partial H / \partial t | m \rangle}{(E_n - E_m)^2} \right| = \left(\sum_{n \neq m} \left| \frac{\hbar \langle n | \partial H / \partial f | m \rangle}{(E_n - E_m)^2} \right| \right) \left| \frac{\partial f}{\partial t} \right|, \quad (\text{S2})$$

where f denotes the frequency of the tunable coupler. Note that the ramping speed of frequency $|df/dt|$ can be modulated with different pulse waveforms. Normally, $|df/dt| \sim 100$ MHz/1 ns in a rapid gate. The energy structure and the corresponding non-adiabaticity factor,

$$\beta = \sum_{n \neq m} \left| \frac{\hbar \langle n | \partial H / \partial f | m \rangle}{(E_n - E_m)^2} \right|, \quad (\text{S3})$$

are then crucial quantities in our discussion.

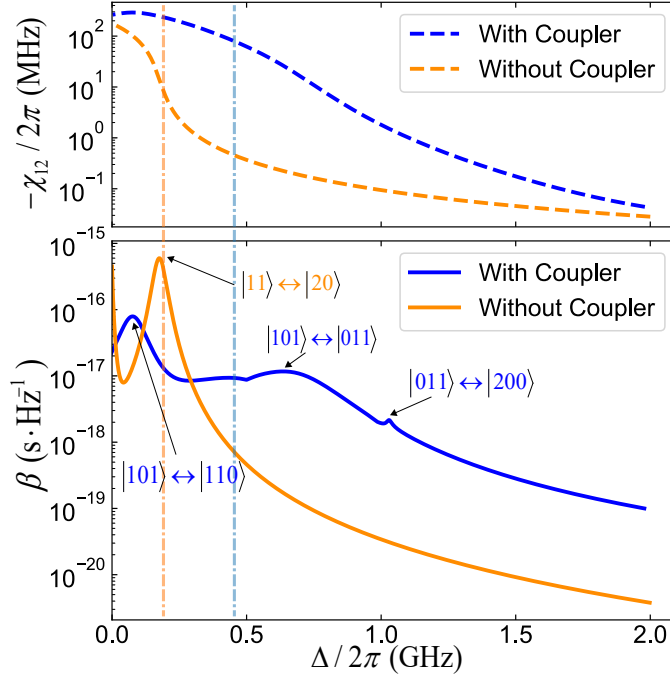


FIG. S3: Simulated ZZ-coupling (top panel) and β_f (bottom panel) versus the frequency detuning Δ . $\Delta = \omega_1 - \omega_2$ in the conventional scheme of using a tunable qubit (orange lines; parameters are from Ref. [4]); $\Delta = \omega_c - \omega_2$ in our scheme of using a tunable coupler (blue lines; parameter are from our device). The dashed vertical lines correspond to the maximum amplitude of the modulation pulses. In the case of using a tunable coupler, β_f is nearly two-orders-of-magnitude smaller in the relevant region for two-qubit interactions, indicating enhanced adiabaticity.

Using the energy structure of our device, we calculate the effective ZZ coupling χ_{12} and the factor β as a function of the coupler frequency, and compare them to the conventional scheme without a tunable coupler (Fig. S3). We find that, with the tunable coupler, the strongest β experienced during the pulse is nearly two-orders-of-magnitude smaller than the conventional scheme, enabling faster and lower-leakage adiabatic controlled-phase gate. Also, we notice that there is a flat response region in β after the coupler being tuned across the higher-frequency Q_1 during the process of our pulse. This suggests that our scheme has intrinsic robustness against instability of control parameters and pulse distortion.

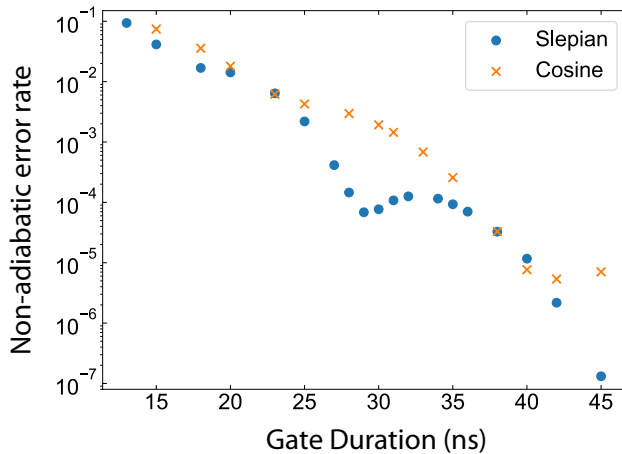


FIG. S4: Simulated non-adiabatic error rate with different gate duration using a cosine and more optimized pulse shape. The simulation is done with an additional 400 MHz Gaussian filter reshaping the pulse. There is no specific optimization for certain gate duration, and the reason for the dip shown around 30 ns in the Slepian case is unknown to us.

As shown in Fig. S4, we performed numerical simulations with the cosine pulse shape used in the experiment, which gives 0.18% non-adiabatic error rate with $\tau_{\text{gate}} = 30$ ns. We also tried alternative pulse shape similar to the original fast adiabatic CZ gate [2]. We find that non-adiabatic errors can be reduced to be below 0.01% with 30 ns gate time. This suggests the potential of this scheme when more coherent qubits become available and the signal distortion can be better remedied.

III. ERROR ANALYSIS

A. Single-qubit gate randomized benchmarking

We perform standard RB experiment for single-qubit gates on both qubits simultaneously. The results are shown in Fig. S5. The average single-qubit gate infidelity is 0.16% for Q_1 and 0.10% for Q_2 .

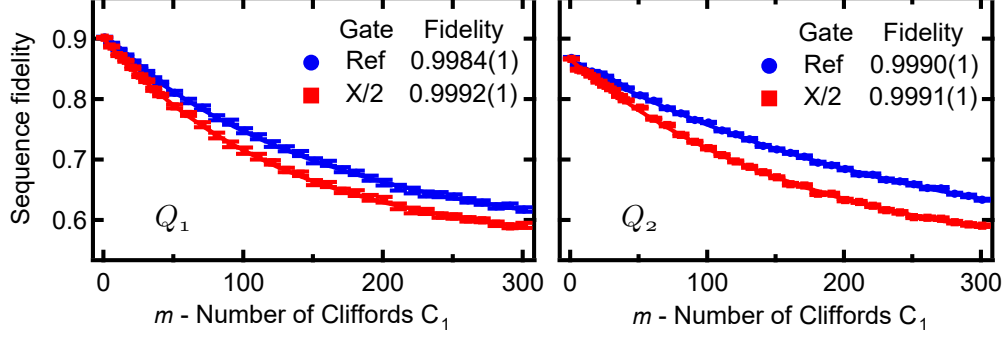


FIG. S5: Simultaneous single-qubit gate RB. Plotted are the sequence fidelity decay for the reference case and the interleaved $X/2$ case.

B. Two-qubit gate randomized benchmarking

The calibrated two-qubit CZ gate is characterized by the conventional Clifford-based RB experiment, with the experimental sequences for both the reference and CZ-interleaved RB experiments shown in the inset of Fig. 3(a) in the main text. The reference RB experiment is performed by applying multiple random sequences composed of two-qubit Clifford gates C_2 , followed by a recovery gate C_r to invert the overall operation. The results are finally averaged over 100 random samples. The CZ-interleaved RB experiment is the same except for an additional CZ gate inserted to each Clifford cycle.

For the conventional two-qubit RB experiments on a two-level system, the ground state probability is measured as the sequence fidelity $P_{00} = \frac{3}{4}p_{\text{depolarized}}^m + \frac{1}{4}$, where m is the number of Clifford gates and $p_{\text{depolarized}}$ is the depolarized error rate, giving the depolarized error per Clifford $r_{\text{depolarized}} = \frac{3}{4}(1 - p_{\text{depolarized}})$. Thus, we perform exponential fit $F = Ap^m + B$ to the two decay curves in Fig. 3(a) in the main text to obtain the two decay constants, p_{ref} and p_{int} , and then the error rate per Clifford, r_{ref} and r_{int} , from $r = \frac{3}{4}(1 - p)$. We can also extract the CZ gate error from $r_{\text{CZ}} = \frac{3}{4}(1 - p_{\text{int}}/p_{\text{ref}})$ and the CZ gate fidelity from $F_{\text{CZ}} = 1 - r_{\text{CZ}}$.

However, when the leakage errors are comparable to other depolarized errors, we need to consider a more complex model of the RB experiment. In this case, the total population occupation of the computational subspace P_s changes as the number of Clifford gates m , $\Delta P_s/\Delta m = -r_{\text{leakage}}P_s + r_{\text{return}}(1 - P_s)$, where r_{leakage} is the leakage rate of the Clifford gate out of the subspace and r_{return} is the total rate from the non-computational states returning back to the subspace. And thus, the final measured ground state probability can be expressed as $P_{00} = \left(\frac{3}{4}p_{\text{depolarized}}^m + \frac{1}{4}\right)P_s$, giving an offset of $\frac{1}{4} \frac{r_{\text{return}}}{r_{\text{return}} + r_{\text{leakage}}}$ for large number of Clifford gates m . Therefore, when the leakage rate r_{leakage} are comparable to the leakage states returning back rate r_{return} , the two-qubit RB traces will not decay to 0.25 and have different offsets, as clearly observed in the experimental data in Fig. 3(a) in the main text.

C. Frequency-dependence of coherence times

The energy relaxation time T_1 and pure dephasing time T_ϕ of qubit Q_1 and Q_2 are measured as a function of coupler frequency, with the experimental results shown in Fig. S6. These measured data are used for generating Fig. 3(b) in the main text. Their effective times during the CZ gate, T_1^{eff} and T_ϕ^{eff} , are obtained by integrating the error rates of energy relaxation (pure dephasing) over different coupler frequencies weighted by the actual half-period cosine pulse shape.

The effective/idling T_1 times are $6.54\mu/10.33\mu\text{s}$ for Q_1 , and $9.48\mu\text{s}/11.88\mu\text{s}$ for Q_2 . The effective/idling T_ϕ times are $0.49\mu\text{s}/8.86\mu\text{s}$ for Q_1 , and $7.21\mu\text{s}/17.63\mu\text{s}$ for Q_2 . Obviously, T_1^{eff} and T_ϕ^{eff} are lower than their counterparts during idling periods (T_1^{idle} and T_ϕ^{idle}). In particular, the higher-frequency qubit Q_1 dephases drastically faster ($T_{\phi,Q_1}^{\text{eff}} \approx 0.5\mu\text{s}$), a consequence of the stronger interaction between the qubit and the less coherent coupler during the CZ pulse.

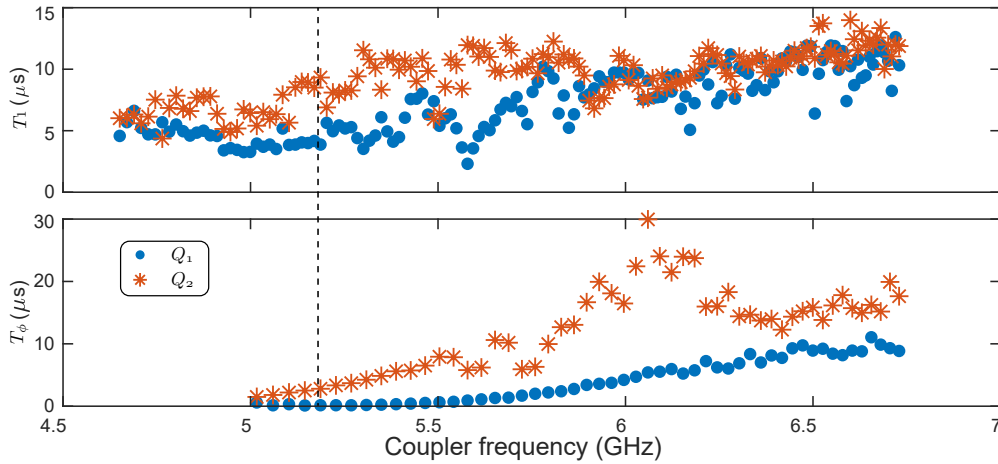


FIG. S6: Energy relaxation (top) and Gaussian pure dephasing (bottom) times v.s. the coupler frequency. The frequency corresponding to the maximum pulse amplitude is marked with the black dashed line.

D. Pulse-induced error

Figure S7 shows the measured data used for generating Fig. 3(c) in the main text. The experiment is used to characterize the extra transitional errors induced by the CZ gate pulse. Note that the extracted transition rates per gate denote the additional errors caused by the CZ pulse, compared to the identity operation. These errors include two parts, additional energy relaxation during gate and transitions caused by the pulse-induced dynamic effect, in this case, the non-adiabatic effect. The experiment is performed on the four initial joint eigen-states $|00\rangle$, $|01\rangle$, $|10\rangle$, and $|11\rangle$, of the two qubits, with the experimental pulse sequence shown in Fig. S7(a) and the corresponding results shown in Fig. S7(b).

Note that the $|00\rangle$ state is supposed to give a flat response, because the adiabatic CZ gate should have almost no effect on the $|00\rangle$ state. However, we still observe a slight rising with pulse number in the measured population. One possible explanation is the CZ pulse may facilitate converting residual thermal or non-equilibrium excited-state populations to the ground state. The pulse-induced transitional error of $|00\rangle$ state is extracted from the difference of the slopes of the two linear fits. For the other three cases, the two population decay curves are fitted with an exponential decay function $F = Ap^m + B$, giving two decay constants p_{Id} and p_{CZ} . The corresponding error rates are extracted by $r = 1 - p_{\text{CZ}}/p_{\text{Id}}$.

The extracted error per gate for each joint state is 0.005%, 0.185%, 0.196%, and 0.316%, respectively, as shown with orange bars in Fig. 3(c) in the main text. These pulse-induced transitional errors include additional energy relaxation during gate and other unwanted transitions coming from the non-adiabatic effects. The additional errors from shortening of energy relaxation times during CZ pulse are calculated by comparing the effective and idling T_1 times of the two qubits and shown with purple bars in Fig. 3(c) in the main text. The average difference between these transitional error rates and the T_1 contribution (orange versus purple bars in Fig. 3(c) in the main text), $(0.06 \pm 0.06)\%$, is thus the non-adiabatic errors. The number undershoots the simulation results presented in Fig. S4, possibly due to the fact that the repeated CZ pulses used in the experiment can produce interference effect, suppressing non-adiabatic errors.

-
- [1] X. Li, T. Cai, H. Yan, Z. Wang, X. Pan, Y. Ma, W. Cai, J. Han, Z. Hua, X. Han, *et al.*, “Tunable coupler for realizing a controlled-phase gate with dynamically decoupled regime in a superconducting circuit,” *Phys. Rev. Applied* **14**, 024070 (2020).
 - [2] J. M. Martinis and M. R. Geller, “Fast adiabatic qubit gates using only σ_z control,” *Phys. Rev. A* **90**, 022307 (2014).
 - [3] R. Barends, J. Kelly, A. Megrant, A. Veitia, D. Sank, E. Jeffrey, T. C. White, J. Mutus, A. G. Fowler, B. Campbell, *et al.*, “Superconducting quantum circuits at the surface code threshold for fault tolerance,” *Nature* **508**, 500 (2014).
 - [4] M. Kjaergaard, M. E. Schwartz, A. Greene, G. O. Samach, A. Bengtsson, M. O’Keeffe, C. M. McNally, J. Braumüller, D. K. Kim, P. Krantz, *et al.*, “A quantum instruction set implemented on a superconducting quantum processor,” [arXiv: 2001.08838](https://arxiv.org/abs/2001.08838) (2020).

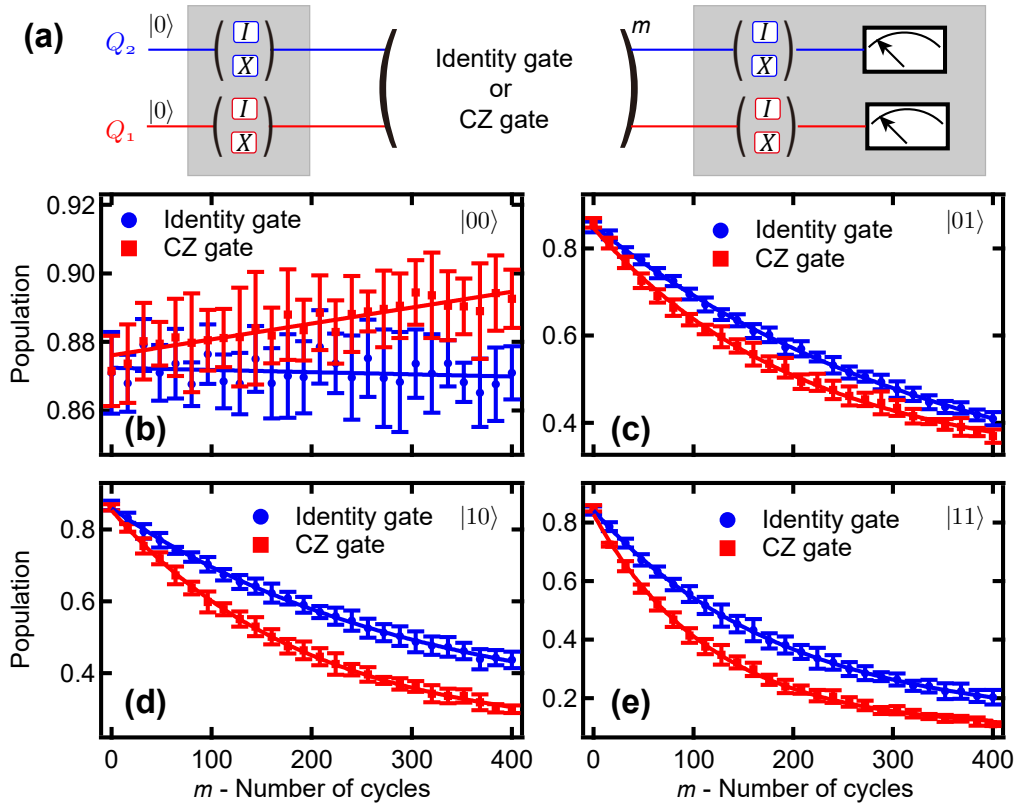


FIG. S7: The pulse-induced errors. (a) The pulse sequence for extracting the pulse-induced errors. A number of m repeated CZ (or Identity) gates are applied. Optional π -pulses before the pulse train are used to prepare the state to $|00\rangle$, $|01\rangle$, $|10\rangle$, and $|11\rangle$. They are inverted back by symmetrically applied π -pulses after the pulse train before measuring the population of the system ground state. (b-e) The measured decay curves (markers) which are exponentially fitted (solid lines) except for the $|00\rangle$ case (linear fit).